Predicting blur visual discomfort for natural scenes by the loss of positional information

Elio D. Di Claudio [a], Paolo Giannitrapani [a,*], Giovanni Jacovitti [b]

[a] Dept. of Information Engineering, Electronics and Telecommunications (DIET), University of Rome "La Sapienza", via Eudossiana 18, I-00184 Rome, Italy
[b] Retired, formerly with DIET, University of Rome "La Sapienza", via Eudossiana 18, I-00184 Rome, Italy

ARTICLE INFO

ABSTRACT

The perception of blur due to accommodation failures, insufficient optical correction or imperfect image reproduction is a common source of visual discomfort, usually attributed to an anomalous and annoying distribution of the image spectrum in the spatial frequency domain. In the present paper, this discomfort is related to a loss of the localization accuracy of the observed patterns. It is assumed, as a starting perceptual principle, that the visual system is optimally adapted to pattern localization in a natural environment. Thus, since the best possible accuracy of the image patterns localization is indicated by the positional Fisher Information, it is argued that blur discomfort is strictly related to a loss of this information. Following this concept, a receptive field functional model is adopted to predict the visual discomfort. It is a complex-valued operator, orientation-selective both in the space domain and in the spatial frequency domain. Starting from the case of Gaussian blur, the analysis is extended to a generic type of blur by applying a positional Fisher Information equivalence criterion. Out-of-focus blur and astigmatic blur are presented as significant examples. The validity of the proposed model is verified by comparing its predictions with subjective ratings. The model fits linearly with the experiments reported in independent databases, based on different protocols and settings.

1. Introduction

Among the various sources of non-clinical visual discomfort (Conlon, Lovegrove, Chekaluk, & Pattison, 1999; Ingrid, 2009; O'Hare, Zhang, Nefs, & Hibbard, 2013), the blur caused by refractive errors is perhaps the most common one.

The discomfort associated with blur is often explained as a consequence of the concentration of the spatial energy spectrum of the perceived image into some bands, or as a byproduct of the discrepancy of this spectrum from the expected spectrum of natural images (O'Hare & Hibbard, 2011; Wilkins, 2016).

Alternative explanations addressed the mismatch of the spatial patterns with the expected ones (Kayargadde & Martens, 1996; Wang & Simoncelli, 2004; Baroncini, Capodiferro, Di Claudio, & Jacovitti, 2009). An in-depth account of previous studies and mathematical models about the blur phenomenon is provided in (Watson & Ahumada, 2011).

Looking at a possible physical mechanism of blur discomfort, three hypotheses are examined in (O'Hare & Hibbard, 2013). The first hypothesis is that discomfort is stimulated by the weak response of the accommodation system. A second hypothesis, somewhat related to the first one, is that discomfort arises because the "micro-fluctuations" observed in the accommodation feedback signal become ineffective (Charman & Heron, 2015; Metlapally, Tong, Tahir, & Schor, 2016; Marin-Franch et al., 2017; Cholewiak, Love, & Banks, 2018). A third hypothesis maintains that, when an image is correctly projected onto the retina, the receptive fields produce a parsimonious, *sparse* representation of this image (McIlhagga & May, 2012). The spatial spread caused by blur excites more receptors, producing a metabolic overload (Juricevic, Land, Wilkins, & Webster, 2010).

In the present approach, the discomfort is quantified in terms of localizability measured by Fisher Information losses. It is argued that, among the basic functions of the human visual system (HVS), detection, recognition, and coarse localization functions are strongly conditioned by the individual experience. Conversely, it seems plausible that the fine localization role is committed to stabler and inter-subjective functions of the HVS.

Based on the above consideration, the present approach starts from postulating that, under normal conditions, the HVS performs the fine localization of the observed patterns with the best accuracy allowed by
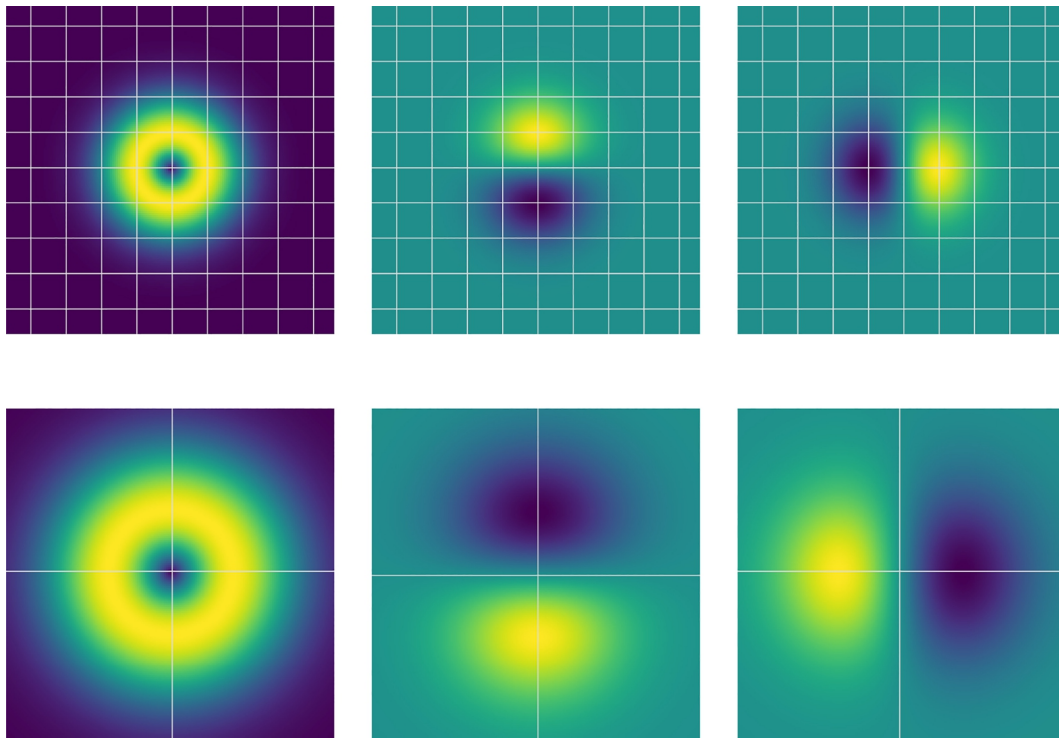

Fig. 1. Upper row: the magnitude of the VRF, its real and imaginary parts referred to the ideal retina grid. Lower row: the magnitude of the VTNF, its real and imaginary parts in the spatial frequency plane. The vertical and horizontal spatial frequencies span the $(-30, 30) cycles/degree$ interval.

its physical macro-structure, given the characteristics of the environment and man's interaction.

This assumption is fundamental, because it is known from the estimation theory that the maximum accuracy attainable when measuring the fine position of patterns in background noise is deduced from the Fisher Information about positional parameters. In fact, the Fisher Information inverse yields the minimum estimation variance (Van Trees, 1992).

Therefore, the focus here is on how the discomfort of blurring is related to the unwanted losses of Positional Fisher Information (PFI) on observed patterns, viewed as *cognitive losses*.

This is a *cognitive approach* because it is inspired to concepts of cognitive sciences and, specifically, the classical Marr's scheme (Marr, 2010). The PFI losses are calculated at the *computational* and *representational* levels, irrespective of the underlying physical mechanisms characterizing the *implementation* level. See (Peebles & Cooper, 2015) and the introduction of (Di Claudio & Jacovitti, 2018).

Therefore, the present approach is agnostic as to whether the discomfort is related to accommodation fatigue or metabolic unbalances. From a more general viewpoint, the cognitive approach may account for the fact that blur discomfort concerns the regions of visual interest (Taylor, 2015) and that the blur is not always undesired or detrimental (Sprague, Cooper, Reissier, Yellapragada, & Banks, 2016). Sometime, the blur is a wanted effect in photography (Datta, Joshi, Li, & Wang, 2006) and microscopy.

Previous analyses of the blur perception phenomenon were mainly oriented to the study of the visual acuity, employing specific stimuli localized either in space, such as edges, lines, crosses, or in the spatial frequency domain, such as sinusoidal gratings, or even in both domains, such as Gabor wavelets (Watson & Ahumada, 2005).

The model presented here is oriented to the evaluation of the visual impact of blur in the vision of *natural scenes*. To this purpose, a generic image projected on the retina is viewed as an element of the *random set* of natural images, characterized by stable statistical features.

The proposed approach is based on an *abstract*, *functional* model of

the receptive fields (RF) of the HVS, allowing for a direct computation of the PFI.

The model accounts, at the same time, for both the contrast sensitivity function (spectral response) and the local directional selectivity of the eye.

For analytical convenience, the blur is modelled as a Gaussian shaped isotropic blur. Then, the analysis is generalized to other types of blur, invoking a criterion of informational equivalence with respect to isotropic Gaussian blur under the PFI paradigm.

To verify the limits of the present approach, the model-based discomfort predictions were first compared to empirical data about the *subjective* quality loss of blurred images, which is arguably related to blur visual discomfort. These data are available in organized databases containing the results of experimental sessions finalized to Image Quality Assessment (IQA), conducted for multimedia industry purposes (Wang, Bovik, Sheikh, & Simoncelli, 2004; ITU, 2008; Bosse, Maniry, Muller, Wiegand, & Samek, 2018). Subsequently, the model is applied to blurred images annotated with ratings of visual discomfort. The results of these experiments confirm the validity of the hypothesis.

The paper is organized as follows. Section 2 describes the features of the functional RF model in the space and in the spatial frequency domains. Section 3 provides the definition of the PFI. In Section 4, the expected Fisher Information acquired during the visual exploration of natural images is computed, and the informational equivalence of a generic blur with a Gaussian isotropic blur is stated. In Section 5, the measure of the visual discomfort is defined. Section 6 presents the comparison of the predicted discomfort with subjective ratings. Some remarks are provided in Section 7. Conclusions are finally drawn in Section 8.

2. The virtual receptive field model

As the luminance plays a dominant role for the localizability of patterns, for the sake of simplicity only the luminance component of the images is accounted for. Chrominance is neglected.
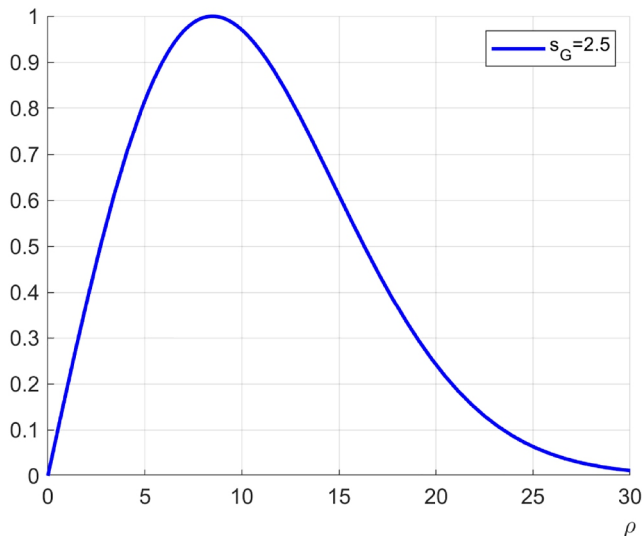
Fig. 2. The radial frequency response magnitude of the VTNF for $s_G = 2.5$ *arcmin* normalized with respect to its maximum value.

The retina in the *foveal vision* is abstractly modeled as a rectangular grid of receptors, whose position is individuated by the coordinate pair $\mathbf{p} \equiv (x_1, x_2)$. Receptors are regularly spaced *one arcmin* apart. The density of 60 *receptors/degree* assures that all the image information within the 30 (=60/2) *cycles/degree* spatial bandwidth is captured by the retina,
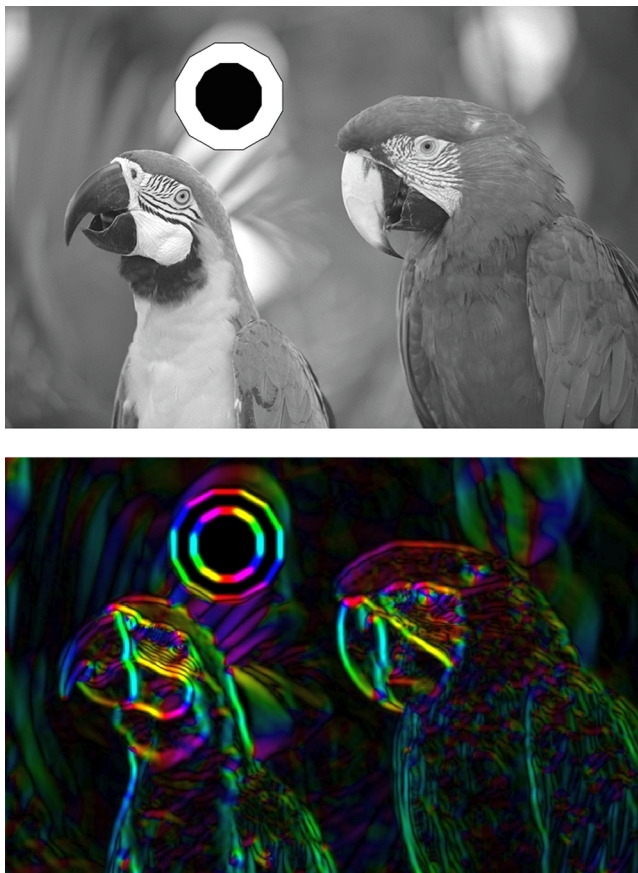

Fig. 3. The luminance of an image (left) of the database LIVE (Sheikh et al., 2006) compared to the corresponding visual map $y(\mathbf{p})$ (right), where the magnitude of the edges is coded into luminance, and their direction, in the interval $[0, \pi)$, into hue. The hue/direction code is read in the edges of the upper-left superimposed polygonal.

according to the Nyquist sampling rule.

For any $\mathbf{p}$, the RF calculates a weighted sum of the luminance $\mathbf{I}(\mathbf{p})$ in a neighborhood of $\mathbf{p}$, yielding a *visual map* $y(\mathbf{p})$. This operation corresponds mathematically to a spatial *convolution*, indicated by the symbol *, between $I(\mathbf{p})$ and the visual map of a single lighting point in the dark, indicated by $h(\mathbf{p})$ and referred to as the Point Spread Function (PSF) of the RF:

$$y(\mathbf{p}) = I(\mathbf{p})*h(\mathbf{p}) \ . \tag{1}$$

The RF model considered here is a harmonic angular filter (HAF). HAF filters are complex valued functions, i.e., they represent *pairs of real filters* (Jacovitti & Cusani, 1990).

With reference to the spatial frequency domain, defined by the horizontal and vertical frequencies f_1, f_2, and to the polar coordinates $\rho = \sqrt{f_1^2 + f_2^2}$ and $\vartheta = \arctan\left(\frac{f_2}{f_1}\right)$, where ρ (Daugman, 1980) is referred to as the *radial frequency* and ϑ is the azimuth, the Fourier spectrum $H(\rho, \vartheta)$ of the RF model is defined as

$$H(\rho, \vartheta) = j2\pi\left(\rho e^{-s_G^2\rho^2} \cdot e^{j\vartheta}\right) \tag{2}$$

where j is the imaginary unit, and s_G is a parameter. This spectrum is *polar separable*, i.e., it is the product of a function of the radial frequency and a function of the azimuth. One outstanding feature of this RF model is that it is also polar separable in the space domain (Daugman, 1983). In fact, taking the inverse Fourier transform of $H(\rho, \vartheta)$, with reference to the space polar coordinates $r = \sqrt{x_1^2 + x_2^2}$ and $\varphi = tg^{-1}\frac{x_2}{x_1}$, the PSF of the RF is:

$$h(r, \varphi) = -2\frac{\pi^3}{s_G^4}\left(re^{-\frac{r^2\pi}{s_G^2}} \cdot e^{j\varphi}\right) \tag{3}$$

which has the same shape of the VNTF, except for a scale factor.

This RF is used herein as a *functional* spatial vision model and, for this reason, it is referred to as *Virtual Receptive Field* (VRF). For short, the term "VRF" will be used in the following to indicate also its PSF and its HAF shape, whereas its Fourier transform $H(\rho, \vartheta)$ will be referred to as Virtual Neural Transfer Function (VNTF), because it represents the *spatial frequency response* of the VRF.

The magnitude and the real components of the VRF are displayed in the upper row of Fig. 1, where the ideal retinal grid is shown in the background. In the same figure, the magnitude, the real and the imaginary parts of the VNTF are displayed in the lower row.

The magnitude of the VNTF frequency response versus the radial frequency is the same in any orientation. It is displayed in Fig. 2. The VNTF is a simple model of the eye contrast sensitivity function.

Here, and from now on, s_G is assumed equal to $s_G = 2.5$ *arcmin*, unless otherwise noted. This choice sets the maximum of the radial frequency response magnitude at about 8.5 *cycles/degree* in the radial frequency, according to the experimental data provided in (Campbell & Green, 1965 & Williams, 1985).

In the lowest spatial frequency range, the magnitude of the VNTF increases linearly. At higher spatial frequencies, the VNTF exhibits a soft-decaying low-pass behavior, reaching an attenuation of about 40 dB at 30 *cycles/degree* at the Nyquist frequency.

This behavior can be interpreted by regarding the VTNF as the cascade of two basic operators:

- an orientation selective *complex gradient* operator $\left(\frac{\partial}{\partial x_1} + j\frac{\partial}{\partial x_2}\right)$ (Reisert & Burkhardt, 2008), whose frequency response is obtained by the Fourier transform derivation rule:

$$j2\pi f_1 + j(j2\pi f_2) = j(2\pi\rho\cos\vartheta + j2\pi\rho\sin\vartheta) = j2\pi\rho e^{j\vartheta} \ ; \tag{4}$$

- a radial frequency selective *Gaussian smoothing* operator, represented by the frequency response:

$$G(\rho, \theta) = e^{-s_G^2 \rho^2} \tag{5}$$

which is responsible of a *neural blur*.

Therefore, the visual map $y(\mathbf{p})$ of the VRF is globally interpreted as a *complex, Gaussian-smoothed gradient field* associated to the retinal image. The parameter s_G will be referred to as the *spread* of the VRF, or as the *neural spread*.

Different from the *complex Gabor* functions, whose paired real components are aligned each other (Daugman, 1993; Watson & Solomon, 1997), the paired real components of the VRF are geometrically orthogonal in the image plane (Fig. 1). As such, the VRF is *steerable* (Simoncelli, Freeman, Adelson, & Heeger, 1992) and more specifically *scalar steerable*, i.e., it rotates in azimuth by multiplication by a complex number as follows

$$h(r, \varphi - \alpha) = h(r, \varphi)e^{j\alpha}$$
$$H(\rho, \vartheta - \alpha) = H(\rho, \vartheta)e^{j\alpha} . \tag{6}$$

This implies that rotated version of the VRFs by a generic azimuth α are obtained by linear combinations of the real components $Re\{h(r, \varphi)\}$ and $Im\{h(r, \varphi)\}$:

$$Re\{h(r, \varphi - \alpha)\} = Re\{h(r, \varphi)\}cos\alpha - Im\{h(r, \varphi)\}sin\alpha$$
$$Im\{h(r, \varphi - \alpha)\} = Re\{h(r, \varphi)\}sin\alpha + Im\{h(r, \varphi)\}cos\alpha . \tag{7}$$

The VRF model materializes into the visual map $y(\mathbf{p})$. In the correspondence of an *edge* of $I(\mathbf{p})$, the magnitude of $y(\mathbf{p})$ measures the *edge strength*, while the phase $tg^{-1}\left[\frac{Im\{y(\mathbf{p})\}}{Re\{y(\mathbf{p})\}}\right]$ indicates the orientation orthogonal to the edge (Jacovitti, 1991; Jacovitti & Neri, 1995; McIlhagga & May, 2012). In the example of Fig. 3, the luminance of a retinal image (left) and its visual map in false color (right) are displayed. In the visual map the gradient strength is indicated by the luminance component whereas, for visual immediateness, only the direction of the gradient in the interval $[0, \pi)$ is indicated with the hue color component.

The visual map $y(\mathbf{p})$ is a *near-complete, sparse representation* of $I(\mathbf{p})$. In fact, except for its mean value, $I(\mathbf{p})$ can be fully recovered from $y(\mathbf{p})$ by *spectral inversion* (i.e., by division by $H(\rho, \vartheta)$ in the frequency domain).

Standard multichannel spatial vision models follow a tomographic-like approach. Around any point, they analyze the image from a limited number of azimuthal views. For each view, they apply co-oriented filters tuned to different bands. Their outputs are then combined in different ways. See (Schütt & Wichmann, 2017) for a historical account.

In comparison, around any point, the VRF performs a full-band *radial tomographic* analysis in every orientation, as described in (Cusani & Jacovitti, 1989; Jacovitti & Cusani, 1990). For the scope of this work, the outstanding advantage of the VRF is that its output (the visual map) allows straightforward computation of the PFI (Neri & Jacovitti, 2004) as described in the next section.

The VRF is the simplest functional spatial vision model based on HAFs. It coincides with the first order component of the orthogonal family of the Laguerre Gauss (LG) functions (Jacovitti & Neri, 2000; Victor & Knight, 2003; Massey & Refregier, 2005) or, equivalently, of the 2D Hermite functions, which span the same signal space (Martens, 1990; Di Claudio, Jacovitti, & Laurenti, 2011). Higher order LG analysis provides *functional* spatial vision models oriented to structures more complex that simple edges (Neri & Jacovitti, 2004; Di Claudio, Jacovitti, & Laurenti, 2010). HAF based *wavelets* can be also used for multi-resolution analysis (Jacovitti & Neri, 2000).

3. The Positional Fisher Information

A *detail* $d_{\mathbf{p}}(\mathbf{q})$ of a visual map $y(\mathbf{p})$ around $\mathbf{p}$ is defined as

$$d_{\mathbf{p}}(\mathbf{q}) = w_{\mathbf{p}}(\mathbf{q}) \cdot y(\mathbf{q} - \mathbf{p}) \tag{8}$$

where $w_{\mathbf{p}}(\mathbf{q})$ is a sampling window.

A comprehensive calculus of the Fisher Information of a detail about its position, orientation, and scale, in the presence of a background Gaussian white noise, was provided in (Neri & Jacovitti, 2004). As specified in (Di Claudio et al., 2010), the *total* PFI of a detail is calculated as:

$$\psi(\mathbf{p}) = \frac{\lambda(\mathbf{p})}{\sigma_V^2} \tag{9}$$

where $\lambda(\mathbf{p})$ is the smoothed gradient energy of the detail, computed as

$$\lambda(\mathbf{p}) = \sum_{\mathbf{q}} w_{\mathbf{p}}(\mathbf{q})^2 |y(\mathbf{q} - \mathbf{p})|^2 \tag{10}$$

and σ_V^2 is the variance of the background noise.[1]

The inverse square root of the PFI

$$e_{MIN}(\mathbf{p}) = \sqrt{\frac{1}{\psi(\mathbf{p})}} = \sqrt{\frac{\sigma_V^2}{\lambda(\mathbf{p})}} \tag{11}$$

represents the minimum standard deviation of the detail position error $e_{MIN}(\mathbf{p})$, achievable with an unbiased estimator, irrespective of the employed estimation method (Van Trees, 1992). Thus, the quantity

$$\sqrt{\psi(\mathbf{p})} = \frac{1}{e_{MIN}(\mathbf{p})} \tag{12}$$

measures the *certainty* of the detail position in the visual plane. For a given amount of background noise, the higher the smoothed gradient energy, the higher the PFI, the greater the certainty about the detail position.

The smoothed gradient energy $\lambda(\mathbf{p})$ is significantly expressed by the (two-dimensional) Fourier transform of the detail. Applying the Parseval theorem (which equates the energy calculated in the space and in the spatial frequency domains) the PFI of the detail represented by its Fourier transform $D_{\mathbf{p}}(\rho, \vartheta)$ is

$$\psi(\mathbf{p}) = \frac{1}{\sigma_V^2} \int_0^{2\pi} \int_0^{+\infty} \rho^2 |G(\rho, \vartheta)|^2 |D_{\mathbf{p}}(\rho, \vartheta)|^2 |B(\rho, \vartheta)|^2 \rho d\rho d\vartheta \tag{13}$$

where $B(\rho, \vartheta)$ is the Optical Transfer Function (OTF), i.e., the spatial frequency response of the optical system, from the observed object to the retina (Watson, 2013). Its inverse 2D transform is the Optical PSF $b(r, \varphi)$.

The overall OTF of a vision system, including the human eye, is a function of the OTFs of cascaded subsystems including the OTF of correcting lenses, the OTF of an imaging system, the OTF of a display system, etc.

Under the hypothesis of linearity, the overall OTF is the product of the single OTFs. In other terms, the overall Optical PSF is the cascaded 2D convolution of the single PSFs.

---

[1] Strictly speaking, the PFI of a detail does not coincide with the PFI of the pattern "contained in" the detail. In fact, the window itself carries its own PFI. In the following, the latter contribution will be neglected, assuming that the window is so smooth that the information carried by its shape is small with respect to the information carried by the captured pattern.

4. The natural scene spectrum and the PFI equivalence

4.1. The PFI of natural scenes

For a generic image, the average PFI calculated on a group of N details visited during the visual exploration is:

$$\frac{\sum_{\mathbf{p}} \lambda(\mathbf{p})}{N\sigma_V^2} = \frac{1}{\sigma_V^2} \int_0^{2\pi} \int_0^{+\infty} \rho^2 |G(\rho,\vartheta)|^2 |D_N(\rho,\vartheta)|^2 |B(\rho,\vartheta)|^2 \rho d\rho d\vartheta \quad (14)$$

where

$$|D_N(\rho,\vartheta)|^2 = \frac{1}{N} \sum_{\mathbf{p}} |D_{\mathbf{p}}(\rho,\vartheta)|^2 \quad (15)$$

is the average energy spectrum of the *N* visited details. The expected value Ψ of the PFI is defined as:

$$\Psi \doteq E\left\{ \frac{\sum_{\mathbf{p}} \lambda(\mathbf{p})}{N\sigma_V^2} \right\} = \frac{1}{\sigma_V^2} \int_0^{2\pi} \int_0^{+\infty} \rho^2 |G(\rho,\vartheta)|^2 E\{|D_N(\rho,\vartheta)|^2\} |B(\rho,\vartheta)|^2 \rho d\rho d\vartheta \quad (16)$$

where $E\{|D_N(\rho,\vartheta)|^2\}$ denotes the expected value of the energy spectrum of the visited details over the random set of natural images.

It is well known that the expected value of the energy spectrum of natural images is proportional to the inverse of the square of the radial frequency, i.e. to $\frac{1}{\rho^2}$. The generality of this spectral distribution is supported by theoretical arguments (Van Der Schaaf & Van Hateren, 1996; Bell & Sejnowski, 1997; Field & Brady, 1997; Simoncelli & Olshausen, 2001; Graham, Chandler, & Field, 2006; Kuang, Poletti, Victor, & Rucci, 2012).

Here, this property is attributed to the *average spectrum* of the *visited details*. Posing, for the sake of generality (Torralba & Oliva, 2003)

$$E\{|D_N(\rho,\vartheta)|^2\} = f(\vartheta)\frac{1}{\rho^2} \quad (17)$$

it follows that

$$\Psi = \frac{1}{\sigma_V^2} \int_0^{2\pi} f(\vartheta) \int_0^{+\infty} |G(\rho,\vartheta)|^2 |B(\rho,\vartheta)|^2 \rho d\rho d\vartheta \quad (18)$$

and, in the absence of blur,

$$\Psi_0 = \frac{1}{\sigma_V^2} \int_0^{2\pi} f(\vartheta) \int_0^{+\infty} |G(\rho,\vartheta)|^2 \rho d\rho d\vartheta . \quad (19)$$

In the case of isotropic Gaussian blur, the OTF is

$$B(\rho,\vartheta) = e^{-s_B^2 \rho^2} \quad (20)$$

where s_B is referred to as the *optical spread*. Therefore,

$$\Psi = \frac{F}{\sigma_V^2} \int_0^{+\infty} e^{-2(s_G^2 + s_B^2)\rho^2} \rho d\rho \quad (21)$$

$$\Psi_0 = \frac{F}{\sigma_V^2} \int_0^{+\infty} e^{-2s_G^2 \rho^2} \rho d\rho \quad (22)$$

where the coefficient *F* is

$$F = \int_0^{2\pi} f(\vartheta) d\vartheta . \quad (23)$$

Finally, from the equality

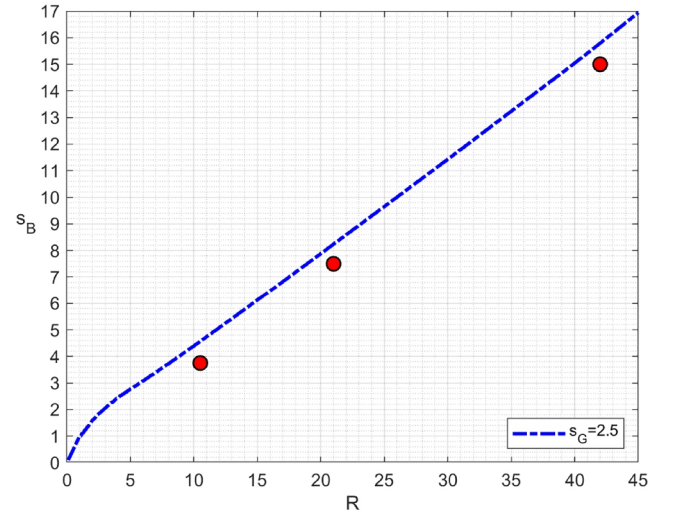$$\int_0^{+\infty} e^{-2(s_G^2 + s_B^2)\rho^2} \rho d\rho = \frac{1}{4(s_G^2 + s_B^2)} \quad (24)$$

Fig. 4. The radius R of the sinc blur versus the spread s_B of its PFI equivalent Gaussian blur. The red circles indicate some average results of experiments conducted with synthetic images emulating natural images (Murray & Bex, 2010).

it follows that

$$\frac{\Psi}{\Psi_0} = \frac{s_G^2}{s_G^2 + s_B^2} . \quad (25)$$

4.2. The PFI equivalence

The above result is so simple owing to the Gaussian shape of the blur. However, having assumed that blur discomfort depends only on the PFI loss, the discomfort due to different types of blur could be predicted by the same formula applying the concept of *PFI equivalence*.

Definition 4.1. (*PFI Equivalence*)   A blur characterized by the generic OTF $B(\rho,\vartheta)$ is said to be PFI equivalent to an isotropic Gaussian blur with standard deviation (spread) s_B if it yields the same expected PFI for natural images, i.e.:

$$\int_0^{2\pi} \int_0^{+\infty} e^{-2s_G^2 \rho^2} |B(\rho,\vartheta)|^2 \rho d\rho d\vartheta = \int_0^{2\pi} \int_0^{+\infty} e^{-2(s_G^2 + s_B^2)\rho^2} \rho d\rho d\vartheta . \quad (26)$$

This equivalence criterion is intuitive. It equals the energies of the actual OTF and of an isotropic Gaussian OTF, both weighted by the squared magnitude of the VNTF. In particular, the PFI equivalence does not depend on the phase of the OTF.

An important example of PFI equivalence is the one of the out-of-focus blur, whose PSF is modeled as a cylinder of unitary volume and radius R. It is referred also to as the *disc blur*, or the *sinc blur*, and is characterized by the following OTF:

$$B(\rho,\vartheta) = 2\frac{J_1(2\pi\rho R)}{2\pi\rho R} . \quad (27)$$

Equating the PFI of the sinc blur and of the Gaussian isotropic blur yields

$$4\int_0^{+\infty} \left(\frac{J_1(2\pi\rho R)}{2\pi\rho R}\right)^2 e^{-2s_G^2\rho^2} \rho d\rho = \int_0^{+\infty} e^{-2(s_G^2 + s_B^2)\rho^2} \rho d\rho = \frac{1}{4(s_G^2 + s_B^2)} . \quad (28)$$

The first integral is not available in closed form. A careful numerical integration provides a value of the optical spread s_B of the isotropic Gaussian blur as a function of its PFI equivalent sinc blur of radius R, as plotted in Fig. 4 and is roughly expressed by the rule $\frac{s_B}{R} \approx \frac{3}{8}$. In the same figure some subjective equivalence judgments averaged over a pool of six observers are also reported. These empirical data refer to synthetic
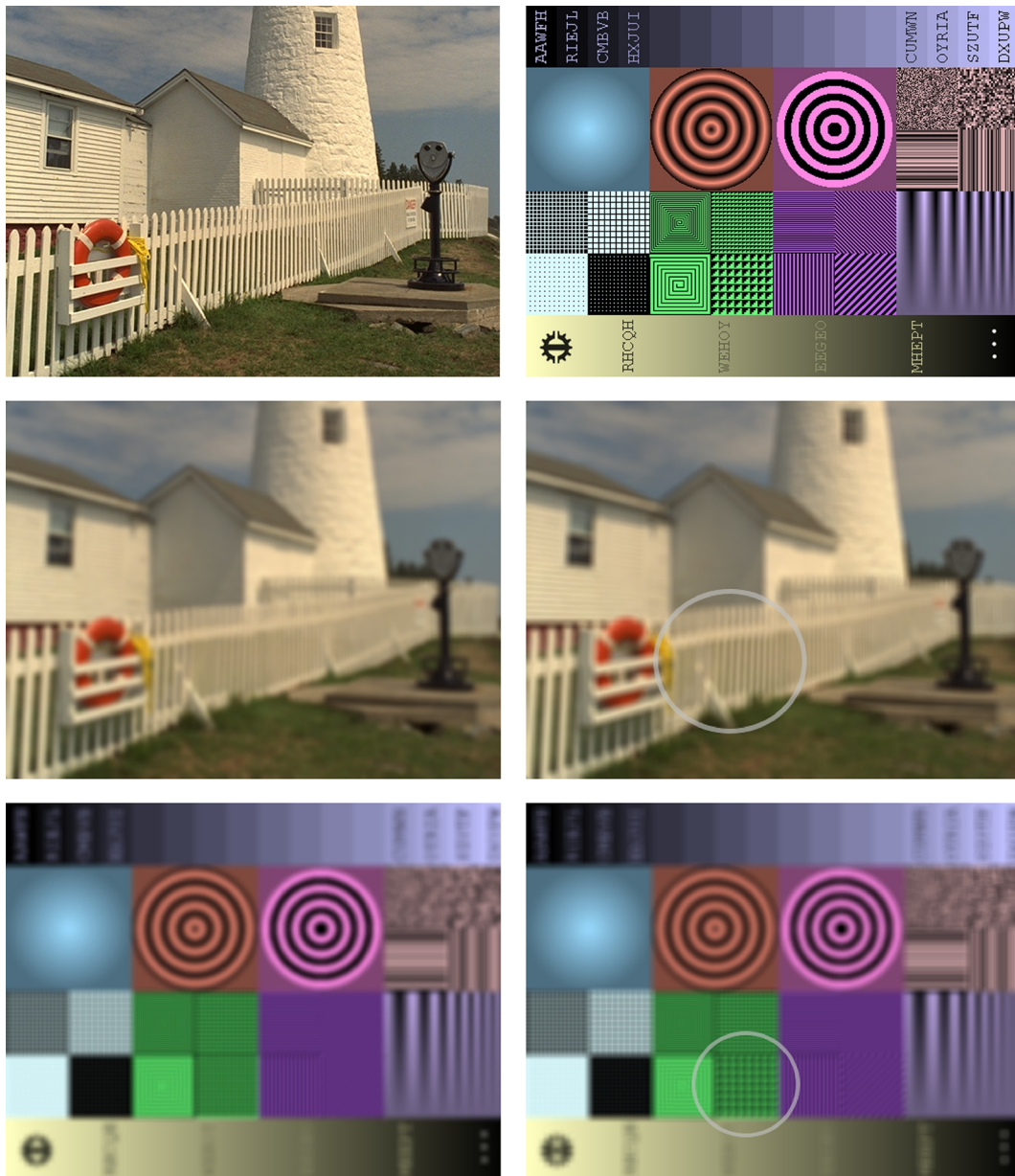
Fig. 5. Upper row: two original images, Second and third rows: Gaussian blurred image (left) and Fisher equivalent sinc blurred images (right). The values of R were chosen to put into evidence the effects of the spectral sidelobes of the sinc blur (see the encircled patterns). Natural image (i19 of the database): $R = 6$ *arcmin*, corresponding to $s_B = 3.1$ *arcmin*. Synthetic image (i25 of the database): $R = 7$ *arcmin*, corresponding to $s_B = 3.4$ *arcmin*.

images whose contours emulate the ones of natural images (Murray & Bex, 2010).

From a perceptual viewpoint, it appears that this equivalence works generally well. Here, to provide the reader with visual examples, the most critical cases in the Tampere image database (TID2013) (Pono-marenko et al., 2015), are reported in Fig. 5, including the non-natural image i25 as a benchmark. Notice that some grating patterns are cancelled out or amplified by the sidelobes of the OTF of the sinc blur in comparison to the Gaussian blur. Notice also that these effects are not present in the natural out-of-focus blur, owing to the apodization of the pupil, which attenuates the sidelobes (Zhang, Ye, Bradley, & Thibos, 1999).

A second example of PFI equivalence regards the non-isotropic Gaussian blur, referred to as *astigmatic* Gaussian blur. For the sake of simplicity, this equivalence is calculated here only for the case of isotropic image spectral energy distribution. Using for convenience the Cartesian coordinates, the OTF of this blur is:

$$B(f_1, f_2) = e^{-2(s_V^2 f_1^2 + s_H^2 f_2^2)} \tag{29}$$

where s_H and s_V are the horizontal and vertical optical spreads. A straightforward algebraic analysis shows that the astigmatic Gaussian blur is PFI equivalent to the isotropic Gaussian blur with spread

$$s_B = \sqrt{\sqrt{s_G^4 + s_G^2(s_H^2 + s_V^2) + s_V^2 s_H^2} - s_G^2} \ . \tag{30}$$

An example is provided in Fig. 6. Two versions of an original image, respectively affected by an astigmatic Gaussian blur with $s_H = 4, s_V = 1$ and with $s_H = 1, s_V = 4$ are compared to the same image affected by their PFI equivalent isotropic Gaussian blur. Notice that the sea waves are better localized in presence of horizontal blur, while masts are better localized in presence of vertical blur. The average localizability loss is visually balanced in the case of the isotropic Gaussian blur.

Fig. 6. A unblurred image (upper left) and its astigmatic blurred versions. For $s_H = 4, s_V = 1$ (horizontal blur, upper right), and for $s_H = 1, s_V = 4$ (vertical blur, lower left). They are PFI equivalent to the isotropic Gassian blurred version shown in the lower right image with $s_B = 2.54$.

5. Prediction of blur discomfort

Provisionally, the amount of blur discomfort is assumed *proportional* to the *relative certainty loss* about the details position[2] defined as:

$$\varepsilon = \frac{\sqrt{\Psi_0} - \sqrt{\Psi}}{\sqrt{\Psi_0}} = 1 - \sqrt{\frac{\Psi}{\Psi_0}} . \tag{31}$$

This assumption is suggested by the belief that the perceived cost of wrong localization is proportional to the uncertainty of the Euclidean distances, at least for small errors.

Then, for the random set of natural images and for isotropic Gaussian blur, using (25) the relative certainty loss takes the form of the following non-dimensional *discomfort index*:

$$\varepsilon = 1 - \sqrt{\frac{\Psi}{\Psi_0}} = 1 - \sqrt{\frac{1}{1 + \left(\frac{s_B}{s_G}\right)^2}} . \tag{32}$$

This index ranges between 0 (in the absence of blur) to 1 (for diverging blur). It depends only on the *normalized blur*, i.e., the ratio between the optical spread on the retinal image and the neural spread of the VRF.

The optical blur spread s_B is subject to change by the action of the natural accommodation system and, in the context of a composite optical system, by the action of technical devices. The neural spread s_G plays instead the role of an inner reference. At glance, it could be argued that it is a stable parameter. However, some experiments indicate that the s_G value is adaptive (Webster, 2002). It appears that the visual adaption to a blurred image causes a dilation of the spread s_G, leading to a reduction of the normalized blur, so that the spectrum of the image
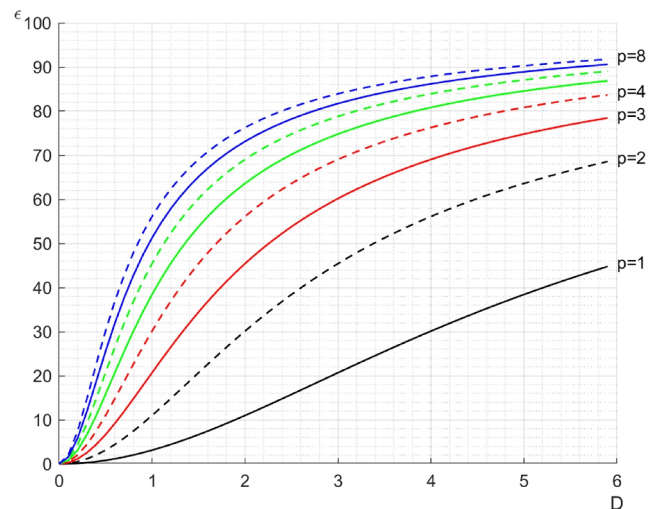

Fig. 7. The value of the theoretical discomfort index in centesimal units versus the diopters (measured in m^{-1}) for different values of the pupil diameter (measured in mm). (A typical pupil diameter when reading at normal illumination is 3 mm).

looks wider and the image sharper.

The discomfort formula is now applied to the blur caused by out-of-focus condition of the eye optics, i.e., in *natural vision*. Using the geometrical arguments of (Strasburger, Bach, & Heinrich, 2018), it is deduced that the radius R of the out-of-focus optical PSF in arcmin is

$$R = 1.71 p |D| \tag{33}$$

where p is the pupil diameter (in mm) and the D is the out-of-focus

---

[2] An exponentiated version of such a measure was employed in (Di Claudio & Jacovitti, 2018).
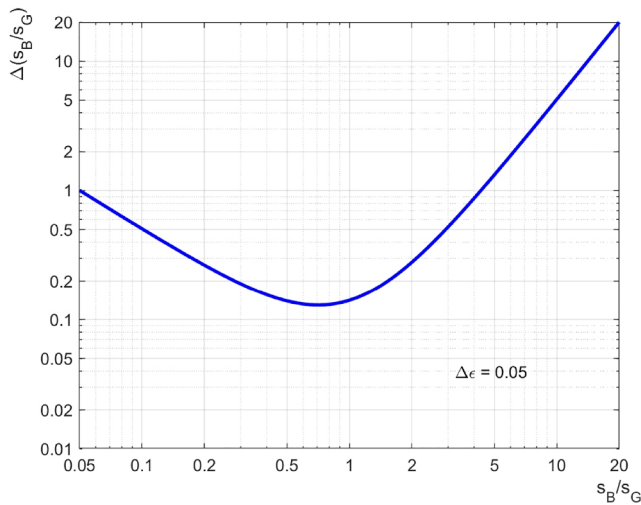
Fig. 8. The theoretical increment $\Delta\left(\frac{s_B}{s_G}\right)$ versus $\frac{s_B}{s_G}$ for $\Delta\varepsilon = 0.05$ in a log/log scale. Curves for different values of $\Delta\varepsilon$ are obtained by vertical translation.

measure in diopter units (m^{-1}).

Applying the $\frac{s_B}{R} \approx \frac{3}{8}$ rule it follows that the spread of the PFI equivalent blur of the out-of-focus blur measured in diopters is approximated as

$$s_B \approx 0.64 p |D| \tag{34}$$

so that a coarse estimate of blur discomfort in natural vision is:

$$\varepsilon = 1 - \sqrt{\frac{1}{1 + \left(0.64 \frac{p}{s_G} D\right)^2}}. \tag{35}$$

In the chart of Fig. 7 this theoretical discomfort index ε is plotted versus D for different pupil diameters. The scale of ε is expressed in centesimal units.

This chart essentially says that, if the out-of-focus discomfort is proportional to the relative certainty loss, as assumed, it is not linear with the blur spread. Moreover, since the sensitivity of the discomfort index with respect to the normalized spread $\xi \doteq \frac{s_B}{s_G}$ is calculated as

$$\frac{d\varepsilon}{d\xi} = \xi \left[\frac{1}{1 + \xi^2}\right]^{\frac{3}{2}} \tag{36}$$

the increment $\Delta\xi$ necessary to produce a given increment $\Delta\varepsilon$ is approximated as:

$$\Delta\xi = \frac{1}{\xi} \left[1 + \xi^2\right]^{\frac{3}{2}} \Delta\varepsilon. \tag{37}$$

This increment exhibits a typical "dipper shape" (Solomon, 2009; O'Hare & Hibbard, 2011) as shown in Fig. 8. The theoretical minimum occurs in the correspondence of the normalized spread value $\xi = \frac{s_B}{s_G} = \frac{1}{\sqrt{2}}$.

In the above formulas, diffraction and aberration contributions to blur discomfort are considered negligible. Non-negligible aberrations could be accounted for by adopting parametric models for characterizing their PSFs (Goodman, 2005; Watson, 2015), and calculating the PFI equivalent blur. A simple example is the aberration due to astigmatic Gaussian blur provided in Section 4, where the blur is characterized by the two parameters s_H and s_V. However, broad generalizations would be quite an undertaking beyond the scope of this paper.

6. Comparison with empirical data

The above results about the phenomenon of blur discomfort for natural images are derived by principles and assumptions. To assess their effectiveness in the reality, the theoretical model was first verified against empirical ratings of the *subjective quality loss* of images caused by blur, which are argued to be strictly related to blur discomfort. These data were released in response to the growing demand by the media industry for reliable automatic image quality assessment (IQA) through objective metrics. Four independent IQA databases were employed, based on different methodologies and protocols, and following different strategies to prevent biases and side effects.

IQA databases include images affected by Gaussian blur, which is considered sufficiently representative of the perceptual effect of the actual blur in many technical applications.

Subsequently, the predictions of the model were compared to experimental data where subjects were literally asked to rate "the *visual discomfort*" due to blur (O'Hare & Hibbard, 2013).

All these experiments do not account for blur discomfort secondary effects, such as psychological consequences that lie behind the scope of the paper. Furthermore, in these experiments the eye optical blur of the observers is corrected if present. So, the blur applied to the observed images emulates an undesired natural optical blur on the retina plane. In fact, under the hypothesis of linearity, the natural optical blur and the artificial blur applied to the observed images are interchangeable, because of the well-known property of cascaded convolutions.

Before presenting the experiments and discussing the results, it is essential to illustrate how the discomfort index must be scaled to fit the experimental settings of a database.

6.1. The Scaled Blur Discomfort Index

To this purpose, the following parametric "Scaled Blur Discomfort Index" (SBDI) is defined from (32):

$$SBDI \doteq a \left[1 - \sqrt{\frac{1}{1 + \left(\gamma^2 \frac{s_B}{s_G}\right)^2}}\right] \tag{38}$$

where the gain *a* fixes the *scoring scale* (Sheikh & Bovik, 2006), and γ is a distance parameter defined as

$$\gamma \doteq \frac{\delta_0}{\delta} \tag{39}$$

where δ_0 is *nominal viewing distance*, i.e., the distance from which the density of pixels projected on the retina matches the previously assumed density of the receptors (60/degree) and δ is the viewing distance adopted in the experiment.

Differently stated, γ equals the ratio between the number of pixels viewed within one degree at distance δ_0 (60 pixels) and the number of pixels viewed within one degree at distance δ.

The role of the distance parameter is understood considering that the VRF spread on the image projected on the retina is $\frac{s_G}{\gamma}$, i.e., it increases proportionally with the viewing distance. Conversely, the projection of the spread of the blur applied to the observed image is γs_B, i.e., it is inversely proportional to the viewing distance.

If not specified, the parameters *a* and γ can be determined from data by regression.

6.2. The "subjective quality loss" experiments

The essential features of the employed IQA databases are illustrated below.

The LIVE Image Quality Assessment Database Release 2 (DBR2) (Sheikh, Sabir, & Bovik, 2006) reports the quality ratings of 779 distorted versions of 29 reference images (included 145 blurred images) from about 23 subjects. Ratings of subjective quality loss with respect to
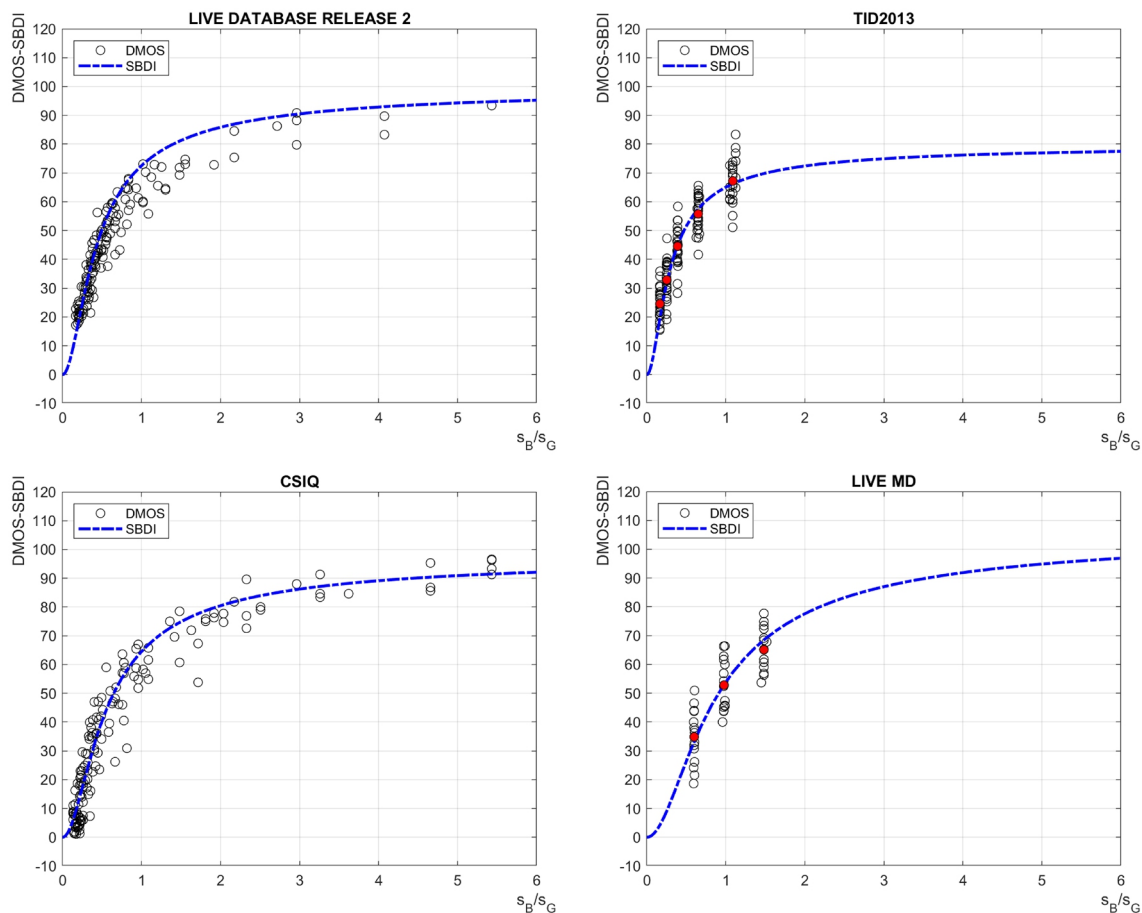
Fig. 9. The empirical DMOS values of the subjective quality loss for the blurred images of the databases versus the normalized blur spread compared to the values predicted by the theoretical model (dashed curves). Averages with respect to images are indicated by the filled circles in the TID2013 and LIVE MD scatterplots.

reference images were expressed on a DMOS (Difference of Mean Opinion Score) scale ranging from 0 (perfect quality) to 100 (absymal quality) using a *double stimulus* strategy.

The Tampere Image Database 2013 (TID2013) (Ponomarenko et al., 2015) contains 3000 distorted images, including 125 blurred images. Quality ratings were collected in five independent labs and on the internet using more than 300 subjects. They were asked to select the *best image between two distorted images* in direct comparison to the reference image. The average quality scores were expressed on a Mean Opinion Score (MOS) scale ranging from 0 (bad quality) to 9 (perfect quality).

The Computational and Subjective Image Quality Database (CSIQ) (Larson & Chandler, 2010) contains 30 reference images and 866 distorted versions, including 150 blurred images. The database includes 5000 ratings of 25 subjects, obtained by *comparative ratings between different images*, reported in DMOS units.

The LIVE Multiply Distorted Image Quality Database (LIVE MD) (Jayaraman, Mittal, Moorthy, & Bovik, 2012) contains 15 reference images and 405 distorted images, including 45 blurred images, whose quality was rated by 37 subjects. The study was conducted using a *single stimulus with hidden reference* strategy, using DMOS scores.

All databases contain images representing *natural scenes*, except the image i25 of the TID2013 database (which was used as a benchmark in Fig. 5).

In the graphs of Fig. 9 the subjective quality loss prediction curves for the blurred images of the different databases are superposed to the empirical DMOS values, plotted versus the normalized spread s_B/s_G. These empirical DMOS data represent *average scores* of the pool of the observers.

In the TID2013 database, ratings are available as MOS values. The DMOS values were inferred considering that the best MOS ratings do not exceed 7.5, as seen from Fig.20 of (Ponomarenko et al., 2015).

Therefore, posing $MOS = 7.5$ in correspondence to $DMOS = 0$ and $MOS = 0$ in correspondence to $DMOS = 100$ yields

$$DMOS = (100/7.5) \times (7.5 - MOS) . \tag{40}$$

In the CISQ database, the DMOS was normalized between its minimum and maximum empirical value.

The blur values of the LIVE MD database were not available. They were estimated through a regularized spectral division of the blurred images with the unblurred ones.

The fitting of the empirical data with the theoretical prediction of the subjective quality loss is substantially linear, as evidenced by the scatterplots of the DMOS empirical ratings versus the predicted ones for all the images contained in the different databases (Fig. 10). In the TID2013 and LIVE MD scatterplots, the averages with respect to the sample images are indicated by filled circles.

In Table 1 the most relevant data about the experimental validation of the model are resumed. The Pearson Linear Correlation Coefficient (PLCC) and the Root Mean Square Error (RMSE) between theoretical and empirical data are also provided. The "claimed" normalized viewing distances were calculated with the information about the experimental settings provided by the respective authors.[3] The sign "–" stands for "not available".[4]

---

[3] The viewing distances of CISQ and LIVE MD are slightly (10%) underestimated. The maximum absolute difference is within ten centimeters. However, the "physical" viewing distance does also depend on the physical dimension of the pixels of the screen.

[4] The Authors are grateful to Prof. Ponomarenko for providing details about the blur settings in the TID2013 database in a personal communication.
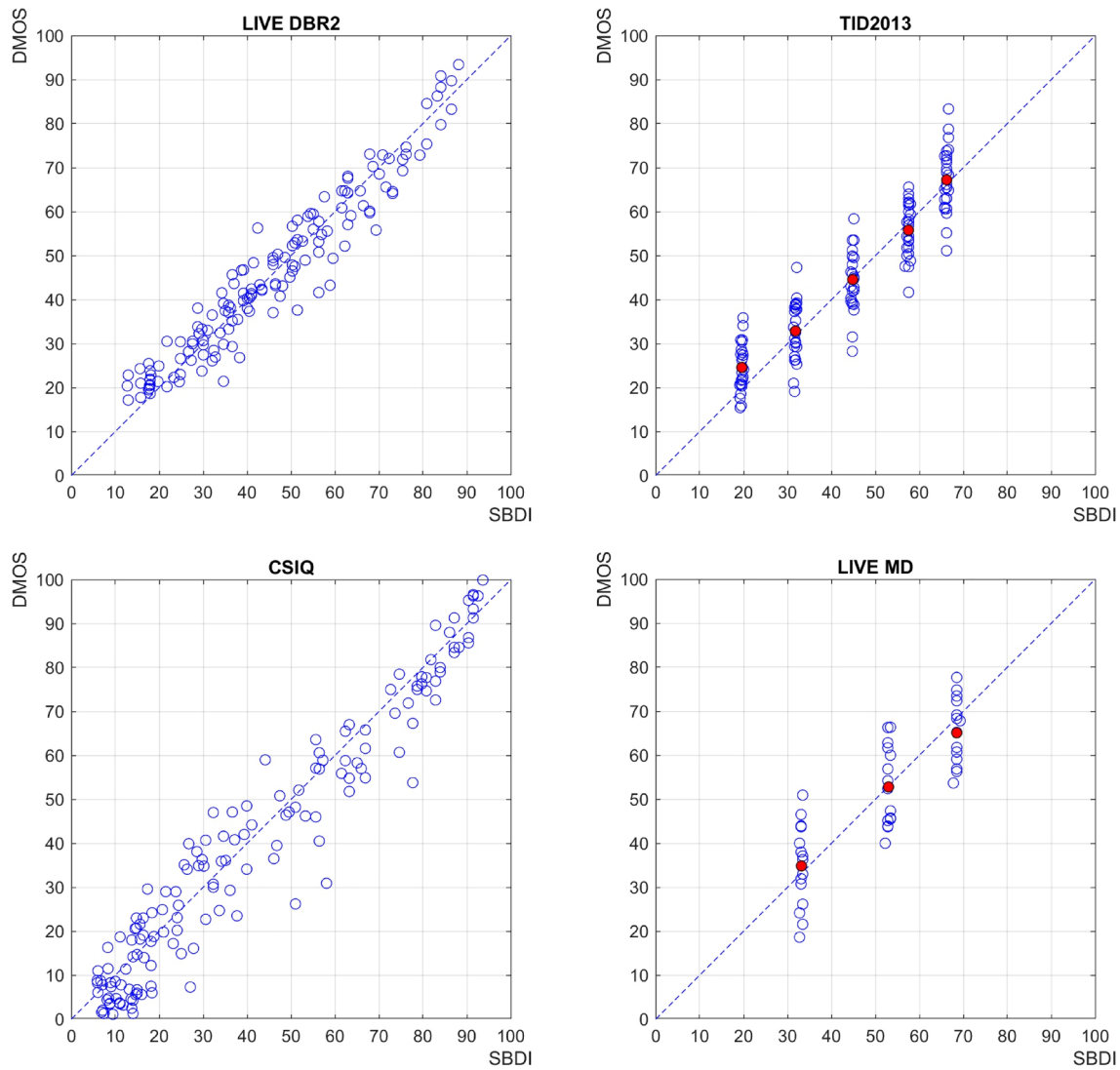
Fig. 10. The scatterplots of the DMOS ratings versus the corresponding SBDI values predicted by the model for each blurred image in the different databases. Averages with respect to images are indicated by filled circles in the TID2013 and LIVE MD scatterplots.

Table 1
Summary of the experimental verification for the four databases and $s_G = 2.5$.

DATABASE	a estimated	$\frac{\delta}{\delta_0}$ claimed	$\frac{\delta}{\delta_0}$ estimated	PLCC	RMSE
LIVE DBR2	93	0.46/0.57	0.53	0.96	5.44
TID2013	80	–	0.44	0.92	6.82
CSIQ	98	0.65	0.60	0.97	7.47
LIVE MD	107	0.84	0.76	0.83	8.57

6.3. The "blur discomfort" experimental data

In (O'Hare & Hibbard, 2013) the results of some experiments aimed to investigate the relationship between visual discomfort judgments and image manipulations causing blur are reported. In particular, "Experiment 3" regards *natural images*.

In these experiments sixty natural images were taken from a database whose images pertain to two general categories: distant natural scenes and closeups natural scenes. In particular, ten images from the first category whose spectral energy has a mean energy spectral radial decay of the kind $\left(\frac{1}{\rho^\beta}\right)^2$ with $\beta = 1.39$, and ten images from the second category, characterized by $\beta = 0.95$, were selected. The scope of this

diversity was to see if visual discomfort judgments would depend on deviation from the ideal spectral slope for natural scenes ($\beta = 1$).

During experimental sessions, thirteen subjects were asked to formulate *discomfort judgments* following a *pairwise comparison* strategy.

Differently from the preceding experiments, ratings are averaged not only over the pool of observers, but also over groups of images. One average regards the distant natural scenes, and the other one regards the closeups natural scenes. As in the TID2013 and in the LIVE MD experiments, few (three) Gaussian blur values were employed, with standard deviations 8, 16, and 32 *cycles/degree* in the spatial frequency domain, corresponding respectively to $s_B = 3.75, s_B = 1.875$ and $s_B = 0.9375$ *arcmin* in the spatial domain. In the Fig. 11 the results of these experiments are reported, along with the discomfort predicted by the SBDI index. The results were expressed in the Thurstone scale (Tsukida & Gupta, 2011), according to the method employed for calculating the discomfort scores, and then converted into the discomfort scale of the SBDI by the following affine transformation:

$$SBDI = 50(Thurstone + 1) . \tag{41}$$

The normalized viewing distance, determined by regression, is $\frac{\delta}{\delta_0} = 0.6$, corresponding to $\gamma = 1.66$.

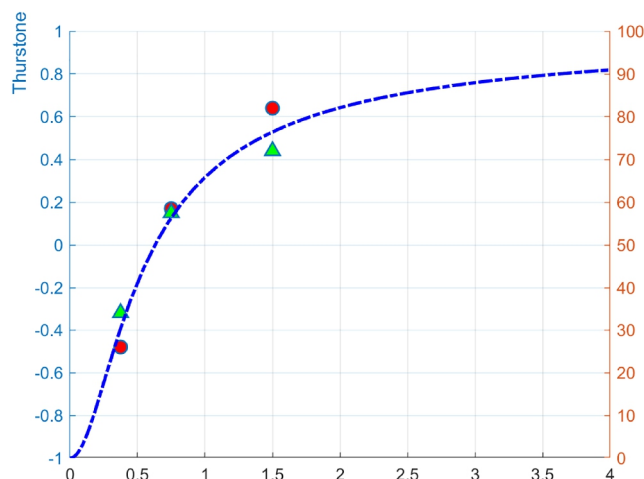The scatterplots of the discomfort ratings versus the normalized

Fig. 11. The scatterplots of the subjective discomfort ratings versus the normalized blur spread for the images in (O'Hare & Hibbard, 2013). The triangles refer to the distant natural scene category, and the circles to the closeups scene category.

Fig. 12. The subjective discomfort ratings versus their theoretical predictions for the images in (O'Hare & Hibbard, 2013). The triangles refer to the distant natural scene category, and the circles to the closeups scene category.
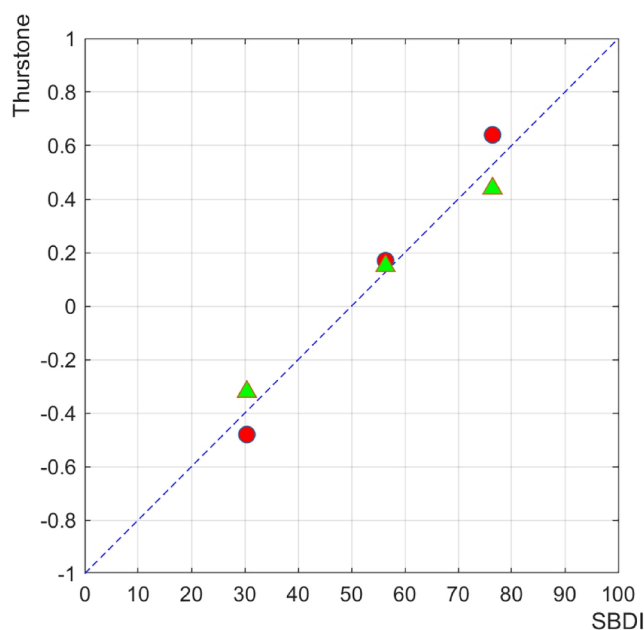
Gaussian blur spread are displayed in Fig. 11 for the groups of images contained in the database, along with the superimposed theoretical prediction curve. The triangles refer to the distant natural scene category, and the circles to the closeups scene category.

The fitting of the empirical data with the theoretical prediction of the subjective quality loss is substantially linear, as evidenced by the scatterplots of the empirical ratings versus the predicted ones for all the images contained in the database (Fig. 12).

The Pearson Linear Correlation Coefficient (PLCC) between the average ratings and the predicted SBDI is 0.98. These results support the argued strict relationship between the subjective quality loss ratings and the visual discomfort ratings caused by blur.

7. Remarks

From the IQA experiments, the judgments expressed by pool of observers for the different natural images appear moderately scattered around the SBDI curve, as indicated by the Root Mean Square Error values of Table 1. This fact is relevant, considering the large variety of the images contained in the databases. This relatively small dispersion can be explained by the adaptive nature of the image exploration, which tends to focus on the details of prominent interest (Baddeley & Tatler, 2006).

This appears even more evident looking at the results of the "blur discomfort" experiments, whose purpose was to verify if the discomfort judgments depend on the deviations from ideal statistics of natural images. The average ratings for selected categories of images characterized by markedly different spectral slopes are so close each other (see Fig. 12), that in (O'Hare & Hibbard, 2013) the authors concluded that the difference among these spectral slopes is not important to blur discomfort judgments.

This evidence underlines the validity of the attribution of the ideal spectrum of natural images to the subset of the visited details. This assumption, made in Section 4, supports the approach followed herein.

However, the image content still influences blur discomfort, as shown by the said moderate, but not negligible, scattering of the subjective ratings in the IQA databases, and as suggested by the common experience. The identification of essential quantitative attributes of images producing different blur discomfort in the presence of the same amount of optical blur is a matter of current investigation.

8. Conclusion

The adoption of a polar separable, complex-valued receptive field model, and of a visual information loss criterion, led to compact theoretical formulas for the prediction of blur visual discomfort for natural scenes, exhibiting a good predictive power faced to several independent experimental data.

- From a general scientific viewpoint, the paper demonstrates that blur discomfort is well correlated with the loss of fine localizability of the observed patterns and with the perceived loss of quality.
- From a system theoretical viewpoint, the approach provides a quantitative prediction of the average psycho-physical findings irrespective of the underlying mechanisms.
- From a technical viewpoint, the results presented here may provide *coarse estimates* of the discomfort caused by undesired blur, for optical correction in natural vision, and for calibration of image reproduction apparatus.

Finally, these results could help in developing IQA methods.[5]

CRediT authorship contribution statement

Elio D. Di Claudio: Validation, Writing - review & editing, Supervision. **Paolo Giannitrapani:** Software, Formal analysis, Visualization. **Giovanni Jacovitti:** Conceptualization, Methodology, Writing - original draft.

Appendix A. Supplementary data

Supplementary data associated with this article can be found, in the

---

[5] For instance, some existing IQA methods model the local smearing of images originated from coding for compression as local blur (Kayargadde & Martens, 1996; Sheikh & Bovik, 2006; Li, Zhang, Ma, & Ngan, 2011; Di Claudio & Jacovitti, 2018). The model developed here may be employed to estimate the contribution of the blur of single details to the overall perceived quality loss.

online version, at https://doi.org/10.1016/j.visres.2021.07.018.

References

Baddeley, R. J., & Tatler, B. W. (2006). High frequency edges (but not contrast) predict where we fixate: A bayesian system identification analysis. *Vision Research, 46*, 2824–2833. https://doi.org/10.1016/j.visres.2006.02.024.

Baroncini, V., Capodiferro, L., Di Claudio, E. D., & Jacovitti, G. (2009). The polar edge coherence: A quasi blind metric for video image quality assessment. In *2009 17th european signal processing conference* (pp. 564–568).

Bell, A. J., & Sejnowski, T. J. (1997). The independent components of natural scenes are edge filters. *Vision Research, 37*, 3327–3338. https://doi.org/10.1016/S0042-6989(97)00121-1.

Bosse, S., Maniry, D., Muller, K., Wiegand, T., & Samek, W. (2018). Deep neural networks for no-reference and full-reference image quality assessment. *IEEE Transactions on Image Processing, 27*, 206–219.

Campbell, F. W., & Green, D. G. (1965). Optical and retinal factors affecting visual resolution. *The Journal of Physiology, 181*, 576–593.

Charman, W. N., & Heron, G. (2015). Microfluctuations in accommodation: an update on their characteristics and possible role. *Ophthalmic and Physiological Optics, 35*, 476–499. https://doi.org/10.1111/opo.12234.

Cholewiak, S. A., Love, G. D., & Banks, M. S. (2018). Creating correct blur and its effect on accommodation. *Journal of Vision, 18*. https://doi.org/10.1167/18.9.1, 1–1.

Conlon, E. G., Lovegrove, W. J., Chekaluk, E., & Pattison, P. E. (1999). Measuring visual discomfort. *Visual Cognition, 6*, 637–663. https://doi.org/10.1080/135062899394085.

Cusani, R., & Jacovitti, G. (1989). A double tomographic approach to the estimation and classification of single objects. In *International conference on acoustics, speech, and signal processing* (pp. 1626–1629, Vol 3). doi: 10.1109/ICASSP.1989.266757.

Datta, R., Joshi, D., Li, J., & Wang, J. Z. (2006). Studying aesthetics in photographic images using a computational approach. In A. Leonardis, H. Bischof, & A. Pinz (Eds.), *Computer Vision – ECCV 2006* (pp. 288–301). Berlin, Heidelberg: Springer, Berlin Heidelberg.

Daugman, J. G. (1980). Two-dimensional spectral analysis of cortical receptive field profiles. *Vision Research, 20*, 847–856. https://doi.org/10.1016/0042-6989(80)90065-6.

Daugman, J. G. (1983). Six formal properties of two-dimensional anisotropic visual filters: structural principles and frequency/orientation selectivity. *IEEE Transactions on Systems, Man, and Cybernetics, 13*, 882–887.

Daugman, J. G. (1993). Quadrature-phase simple-cell pairs are appropriately described in complex analytic form. *Journal of the Optical Society of America, 10*, 375–377. https://doi.org/10.1364/JOSAA.10.000375.

Di Claudio, E. D., & Jacovitti, G. (2018). A detail-based method for linear full reference image quality prediction. *IEEE Transactions on Image Processing, 27*, 179–193.

Di Claudio, E. D., Jacovitti, G., & Laurenti, A. (2010). Maximum Likelihood orientation estimation of 1-D patterns in Laguerre-Gauss subspaces. *IEEE Trans. on Image Processing, 19*, 1113–1125.

Di Claudio, E. D., Jacovitti, G., & Laurenti, A. (2011). On the inter-conversion between Hermite and Laguerre local image expansions. *IEEE Transactions on Image Processing, 20*, 3553–3565.

Field, D. J., & Brady, N. (1997). Visual sensitivity, blur and the sources of variability in the amplitude spectra of natural scenes. *Vision Research, 37*, 3367–3383. https://doi.org/10.1016/S0042-6989(97)00181-8.

Goodman, J. W. (2005). Introduction to fourier optics. Introduction to Fourier optics, 3rd ed., by JW Goodman. Englewood, CO: Roberts & Co., Publishers, 2005 1.

Graham, D. J., Chandler, D. M., Field, D. J. (2006). Can the theory of whitening explain the center-surround properties of retinal ganglion cell receptive fields? *Vision Research, 46*, 2901–2913.

Ingrid, L. M., .I.W..F.M..H., 2009. Visual discomfort and visual fatigue of stereoscopic displays: A review. *Journal of Imaging Science and Technology. 53*, 30201-1–30201-14 (14).

ITU. (2008). *Subjective video quality assessment methods for multimedia applications*. International Telecommunication Union.

Jacovitti, G., & Cusani, R. (1990). Local angular spectrum analysis of 2d signals. In *Fifth ASSP workshop on spectrum estimation and modeling* (pp. 54–58).

Jacovitti, G., & Neri, A. (1995). Bayesian removal of coding-block artifacts in the harmonic-angular filters features domain. In *Proc. SPIE, nonlinear image processing VI, San Jose, CA, USA* (pp. 139–150).

Jacovitti, G., & Neri, A. (2000). Multiresolution circular harmonic decomposition. *IEEE Transactions on Signal Processing, 48*, 3242–3247.

Jacovitti, R. C. G. (1991). Contour coding of still pictures by harmonic angular filters. In *Proc. int. conf. digital signal processing* (pp. 362–365).

Jayaraman, D., Mittal, A., Moorthy, A. K., & Bovik, A. C. (2012). Objective quality assessment of multiply distorted images. In *2012 Conference record of the forty sixth asilomar conference on signals, systems and computers (ASILOMAR)* (pp. 1693–1697).

Juricevic, I., Land, L., Wilkins, A., & Webster, M. A. (2010). Visual discomfort and natural image statistics. *Perception, 39*, 884–899.

Kayargadde, V., & Martens, J. (1996). Perceptual characterization of images degraded by blur and noise: model. *Journal of the Optical Society of America A, Optics, Image Science, and Vision, 13*, 1178–1188.

Kuang, X., Poletti, M., Victor, J. D., & Rucci, M. (2012). Temporal encoding of spatial information during active visual fixation. *Current Biology, 22*, 510–514. https://doi.org/10.1016/j.cub.2012.01.050.

Larson, E. C., & Chandler, D. M. (2010). Most apparent distortion: full-reference image quality assessment and the role of strategy. *Journal of Electronic Imaging, 9*, 011006/1–21.

Li, S., Zhang, F., Ma, L., & Ngan, K. N. (2011). Image quality assessment by separately evaluating detail losses and additive impairments. *IEEE Transactions on Multimedia, 13*, 935–949. https://doi.org/10.1109/TMM.2011.2152382.

Marin-Franch, I., Aguila-Carrasco, A. J. D., Bernal-Molina, P., Esteve-Taboada, J. J., Lopez-Gil, N., Montes-Mico, R., & Kruger, P. B. (2017). There is more to accommodation of the eye than simply minimizing retinal blur. *Biomedical Optics Express, 8*, 4717–4728. https://doi.org/10.1364/BOE.8.004717.

Marr, D. (2010). *Vision: A computational investigation into the human representation and processing of visual information*. The MIT Press.

Martens, J. B. (1990). The Hermite transform – Theory. *IEEE Transactions on Acoustic Speech and Signal Processing, 38*, 1595–1606.

Massey, R., & Refregier, A. (2005). Polar shapelets. *Monthly Notices of the Royal Astronomical Society, 363*, 197–210.

McIlhagga, W. H., & May, K. A. (2012). Optimal edge filters explain human blur detection. *Journal of Vision, 12*. https://doi.org/10.1167/12.10.9, 9–9.

Metlapally, S., Tong, J. L., Tahir, H. J., & Schor, C. M. (2016). Potential role for microfluctuations as a temporal directional cue to accommodation. *Journal of Vision, 16*. https://doi.org/10.1167/16.6.19, 19–19.

Murray, S., & Bex, P. (2010). Perceived blur in naturally contoured images depends on phase. *Frontiers in Psychology, 1*, 185. https://doi.org/10.3389/fpsyg.2010.00185.

Neri, A., & Jacovitti, G. (2004). Maximum likelihood localization of 2-D patterns in the Gauss-Laguerre transform domain: theoretic framework and preliminary results. *IEEE Transactions on Image Processing, 13*, 72–86. https://doi.org/10.1109/TIP.2003.818021.

O'Hare, L., & Hibbard, P. B. (2011). Spatial frequency and visual discomfort. *Vision Research, 51*, 1767–1777. https://doi.org/10.1016/j.visres.2011.06.002.

O'Hare, L., & Hibbard, P. B. (2013). Visual discomfort and blur. *Journal of Vision, 13*. https://doi.org/10.1167/13.5.7, 7–7.

O'Hare, L., Zhang, T., Nefs, H. T., & Hibbard, P. B. (2013). Visual discomfort and depth-of-field. *i-Perception, 4*, 156–169. https://doi.org/10.1068/i0566. pMID: 23799193.

Peebles, D., & Cooper, R. P. (2015). Thirty years after marr's vision: Levels of analysis in cognitive science. *Topics in Cognitive Science, 7*, 187–190. https://doi.org/10.1111/tops.12137.

Ponomarenko, N., Jin, L., Ieremeiev, O., Lukin, V., Egiazarian, K., Astola, J., Vozel, B., Chehdi, K., Carli, M., Battisti, F., & Kuo, C. C. J. (2015). Image database TID2013: Peculiarities, results and perspectives. *Signal Processing: Image Communication, 30*, 57 – 77. doi: https://doi.org/10.1016/j.image.2014.10.009.

Reisert, M., & Burkhardt, H. (2008). Complex derivative filters. *IEEE Transactions on Image Processing, 17*, 2265–2274.

Schütt, H. H., & Wichmann, F. A. (2017). An image-computable psychophysical spatial vision model. *Journal of Vision, 17*. https://doi.org/10.1167/17.12.12, 12–12.

Sheikh, H. R., & Bovik, A. C. (2006). Image information and visual quality. *IEEE Transactions on Image Processing, 15*, 430–444.

Sheikh, H. R., Sabir, M. F., & Bovik, A. C. (2006). A statistical evaluation of recent Full Reference image quality assessment algorithms. *IEEE Transactions on Image Processing, 15*, 3441–3452. URL: live.ece.utexas.edu/research/quality/subjective.htm.

Simoncelli, E. P., Freeman, W. T., Adelson, E. H., & Heeger, D. J. (1992). Shiftable multi-scale transforms. *IEEE Transactions om Information Theory, 38*, 587–607 (Special Issue on Wavelets).

Simoncelli, E. P., & Olshausen, B. A. (2001). Natural image statistics and neural representation. *Annual Review of Neuroscience, 24*, 1193–1216. https://doi.org/10.1146/annurev.neuro.24.1.1193.

Solomon, J. A. (2009). The history of dipper functions. *Attention, Perception, Psychophysics, 71*, 435–443.

Sprague, W. W., Cooper, E. A., Reissier, S., Yellapragada, B., & Banks, M. S. (2016). The natural statistics of blur. *Journal of Vision, 16*, 23.

Strasburger, H., Bach, M., & Heinrich, S. P. (2018). Blur unblurred - a mini tutorial. *i-Perception, 9*, 2041669518765850. doi: 10.1177/2041669518765850. pMID: 29770182.

Taylor, C. P. B. P. (2015). On the number of perceivable blur levels in naturalistic images. *Vision Research, 115*, 142–150.

Torralba, A., & Oliva, A. (2003). Statistics of natural image categories. *Network: Computation in Neural Systems, 14*, 391–412. doi: 10.1088/0954-898X_14_3_302. pMID: 12938764.

Tsukida, K., & Gupta, M. R. (2011). How to analyze paired comparison data. *Technical Report*. UWEETR-2011-0004.

Van Der Schaaf, A., & Van Hateren, J. H. (1996). Modelling the power spectra of natural images: statistics and information. *Vision Research, 36*, 2759–2770. https://doi.org/10.1016/0042-6989(96)00002-8.

Van Trees, H. L. (1992). *Detection, estimation, and modulation theory: Radar-sonar signal processing and gaussian signals in noise*. USA: Krieger Publishing Co., Inc.

Victor, J. D., & Knight, B. W. (2003). Simultaneously band and space limited functions in two dimensions, and receptive fields of visual neurons. In E. Kaplan, J. Marsden, K. R. Sreenivasan (Eds.), *Springer applied mathematical sciences series* (pp. 375–420). New York: Springer-Verlag.

Wang, Z., Bovik, A. C., Sheikh, H. R., & Simoncelli, E. P. (2004). Image quality assessment: From error visibility to structural similarity. *IEEE Transactions on Image Processing, 13*, 600–612.

Wang, Z., & Simoncelli, E. P. (2004). Local phase coherence and the perception of blur. In S. Thrun, L. K. Saul, & B. Scholkopf (Eds.), *Advances in neural information processing systems 16* (pp. 1435–1442). MIT Press.

Watson, A. B. (2013). A formula for the mean human optical modulation transfer function as a function of pupil size. *Journal of Vision, 13*, 18.

Watson, A. B. (2015). Computing human optical point spread functions. *Journal of Vision, 15*. https://doi.org/10.1167/15.2.26, 26–26.

Watson, A. B., & Ahumada, A. J. (2011). Blur clarified: A review and synthesis of blur discrimination. *Journal of Vision, 11*. https://doi.org/10.1167/11.5.10, 10–10.

Watson, A. B., & Ahumada, A. J. (2005). A standard model for foveal detection of spatial contrast. *Journal of Vision 5*, 6–6. doi: 10.1167/5.9.6.

Watson, A. B., & Solomon, J. A. (1997). Model of visual contrast gain control and pattern masking. *Journal of the Optical Society of America A, 14*, 2379–2391. https://doi.org/10.1364/JOSAA.14.002379.

Webster, M. A. G. M. W. S. (2002). Neural adjustments to image blur. *Nature Neuroscience, 5*, 839–840. doi: 10.1038/nn906.

Wilkins, A. (2016). A physiological basis for visual discomfort: Application in lighting design. *Lighting Research & Technology, 48*, 44–54. https://doi.org/10.1177/1477153515612526.

Williams, D. R. (1985). Visibility of interference fringes near the resolution limit. *Journal of the Optical Society of America A, 2*, 1087–1093. https://doi.org/10.1364/JOSAA.2.001087.

Zhang, X., Ye, M., Bradley, A., & Thibos, L. (1999). Apodization by the stiles–crawford effect moderates the visual impact of retinal image defocus. *Journal of the Optical Society of America A, 16*, 812–820. https://doi.org/10.1364/JOSAA.16.000812.